

# Paths to caustic formation in turbulent aerosols

Jan Meibohm,<sup>1</sup> Vikash Pandey,<sup>2</sup> Akshay Bhatnagar,<sup>3</sup> Kristian Gustavsson,<sup>1</sup> Dhruvadya Mitra,<sup>3</sup> Prasad Perlekar,<sup>2</sup> and Bernhard Mehlig<sup>1</sup>

<sup>1</sup>*Department of Physics, Gothenburg University, SE-41296 Gothenburg, Sweden*

<sup>2</sup>*TIFR Centre for Interdisciplinary Sciences, Tata Institute of Fundamental Research, Gopanpally, Hyderabad 500046, India*

<sup>3</sup>*NORDITA, Royal Institute of Technology and Stockholm University, Roslagstullsbacken 23, SE-10691 Stockholm, Sweden*

The dynamics of small yet heavy, identical particles in turbulence exhibits singularities, called caustics, that lead to large fluctuations in the spatial particle-number density, and in collision velocities. For large particle inertia the fluid velocity at the particle position is essentially a white-noise signal and caustic formation is analogous to Kramers escape. Here we show that caustic formation at small particle inertia is different. Caustics tend to form in the vicinity of particle trajectories that experience a specific history of fluid-velocity gradients, characterised by low vorticity and violent strains exceeding a large threshold. We develop a theory that explains our findings in terms of an optimal path to caustic formation, that is approached in the small inertia limit.

Ensembles of heavy particles in turbulence exhibit large fluctuations of the particle-number density and of their relative velocities [1–4]. These fluctuations are enhanced by the formation of caustics [5–7], folds of the particle distribution over configuration space. Caustic formation is an effect of particle inertia, driven by the fluid-velocity gradients, that gives rise to a multi-valued particle-velocity field. Due to this multi-valuedness, often called ‘sling effect’ [8, 9], particles may approach each other, and possibly collide, at large relative velocities. Accordingly, caustics have an important impact on the distribution of relative velocities [10–13], and are a crucial ingredient to theories for collision rates and collision outcomes [14–16].

Caustics have been extensively studied in direct numerical simulations (DNS) of particles in turbulence [9] and model flows [6, 17–22]. Recent numerical studies [23, 24] found that high-velocity collisions tend to occur where the turbulent strain is large, but this cannot be explained in terms of the white-noise models usually used to study caustic formation [5–7]. A precise understanding of how caustics form at small particle inertia, including the local flow conditions that lead to their formation, is crucial for the identification of caustics in experiments [25], and for sampling them efficiently in DNS [9].

In this Letter, we describe a significant step towards a detailed understanding of how caustics form in turbulence. Using DNS of two-dimensional turbulence we show that whether a caustic forms or not depends on the history of fluid-velocity gradients experienced by closely particles, not just upon instantaneous correlations between particle positions and flow gradients (preferential concentration [4, 26, 27]). When particle inertia is small we find a most likely history, an ‘optimal path’ to caustic formation. To determine this path is an optimal-fluctuation problem, similar in nature to localisation due to optimal potential fluctuations in disordered conductors [28], population extinction due to environmental and population-size fluctuations [29, 30], and shock formation in Burgers turbulence [31, 32]. Based on this observa-

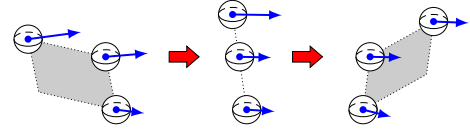


FIG. 1. Illustration of caustic formation in two dimensions. A caustic is formed when the area  $\hat{\mathcal{V}}$  of the parallelepiped spanned by three nearby particles, shown in grey, vanishes.

tion, we develop a theory that explains how the strain and vorticity change along the optimal path to caustic formation: The fluid strain performs a time-localised, violent fluctuation that exceeds a large threshold, while vorticity remains small. Our results explain qualitatively why DNS of particles in turbulence show increased collision rates in straining regions [23, 24]. Even at finite inertia, the optimal path leaves a clear mark in the data, providing criteria for the identification, and the efficient sampling, of caustics in experiments and in DNS.

In a dilute suspension of small, heavy, spherical particles the dynamics of a single particle is approximately given by Stokes’ law [4]

$$\frac{d}{dt}\mathbf{x}(t) = \mathbf{v}(t), \quad \frac{d}{dt}\mathbf{v}(t) = \tau_p^{-1}\{\mathbf{u}[\mathbf{x}(t), t] - \mathbf{v}(t)\}. \quad (1)$$

Here  $\mathbf{x}$  and  $\mathbf{v}$  denote particle position and velocity,  $\tau_p = 2a^2\rho_p/(9\rho_f\nu)$  is the particle-relaxation time which depends on the particle size  $a$ , the kinematic viscosity  $\nu$  of the fluid, and upon the particle and fluid densities,  $\rho_p$  and  $\rho_f$ . The turbulent fluid-velocity field, evaluated at the particle position, is denoted by  $\mathbf{u}[\mathbf{x}(t), t]$ .

To describe caustic formation, consider the parallelepiped spanned by  $d + 1$  nearby particles in  $d$  spatial dimensions. How the spatial volume  $\hat{\mathcal{V}}(t)$  of this object contracts or expands under the non-linear dynamics (1) is determined by the spatial Jacobian  $J_{ij}[\mathbf{x}(t_0), t] = \partial x_i(t)/\partial x_j(t_0)$ , namely  $\hat{\mathcal{V}}(t) = |\det J(t)|$ . Since the dynamics (1) takes place in  $2d$ -dimensional phase-space, spatial sub-volumes  $\hat{\mathcal{V}}$  may collapse in finite time,  $\hat{\mathcal{V}} \rightarrow 0$ , when a caustic forms [4]. Figure 1 shows a typical

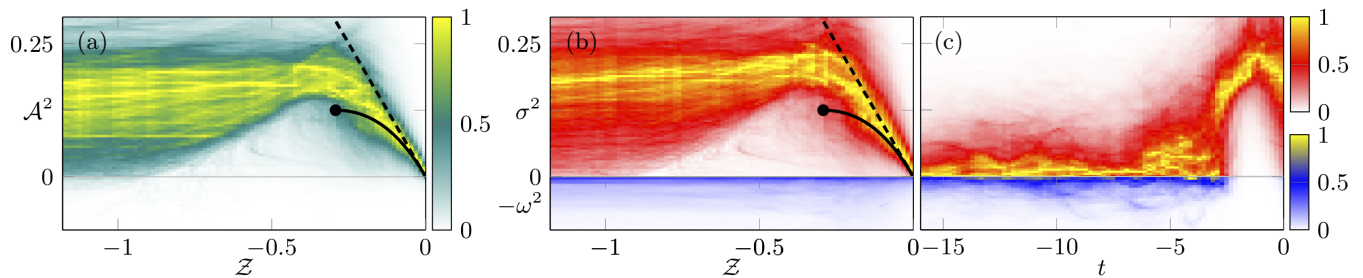


FIG. 2. Path to caustic formation for  $St = 0.31$ . Numerical results using DNS of two-dimensional turbulence. The path density is colour-coded, normalised to unity along each vertical slice to improve visibility. (a) Path density in the  $Z$ - $\mathcal{A}^2$ -plane. The dashed line shows the perturbative approximation,  $Z \sim -\mathcal{A}^2$ , in dimensionless coordinates. The solid line shows the evolution stable fixed point according to Eq. (6), the dot marks the bifurcation point (see main text). (b) Individual contributions from strain ( $Z$  vs.  $\sigma^2$ , positive axis) and vorticity ( $Z$  vs.  $-\omega^2$ , negative axis). (c) Path densities for  $\sigma^2$  (positive axis) and  $-\omega^2$  (negative axis) as a function of time before caustics form at  $t = 0$ .

particle configuration that leads to a caustic in two spatial dimensions. As is well known, caustic formation is closely related to the dynamics of the particle-velocity gradients, which reads in dimensionless form [4, 8]

$$\text{St} \frac{d}{dt} \mathbb{Z}(t) = -\mathbb{Z}(t) - \mathbb{Z}(t)^2 + \mathbb{A}(t). \quad (2)$$

Here  $Z_{ij} = \tau_p \partial v_i(t) / \partial x_j(t)$  and  $A_{ij} = \tau_p \partial u_i(t) / \partial x_j(t)$ , are the dimensionless matrices of particle-velocity gradients and fluid-velocity gradients, respectively. In Eq. (2) time is dedimensionalised by the Kolmogorov time scale,  $\tau_K = \tau_p \langle \text{Tr} \mathbb{A} \mathbb{A}^T \rangle^{-1/2}$ , and the initial condition for  $\mathbb{Z}$  is  $\mathbb{Z}(t_0) = \mathbb{A}(t_0)$ . Here and in the following, we use the abbreviations  $\mathbb{Z}(t) = \mathbb{Z}[\mathbf{x}(t), t]$  and  $\mathbb{A}(t) = \mathbb{A}[\mathbf{x}(t), t]$ . Using (2) one finds [4]

$$\hat{\mathcal{V}}(t) = \hat{\mathcal{V}}(t_0) \exp \int_{t_0}^t ds \mathbb{Z}(s), \quad (3)$$

where  $\mathcal{Z} = \text{Tr} \mathbb{Z}$  is the divergence of the field of particle-velocity gradients. Hence, a necessary condition for caustic formation is that  $\mathcal{Z}$  escapes to negative infinity.

Apart from the Reynolds number  $Re$  that specifies the turbulence intensity, the particle dynamics is determined by the Stokes number  $St = \tau_p / \tau_K$ , a dimensionless measure of particle inertia. For small  $St$ , particle detachment is characterised by  $\mathbb{A} - \mathbb{Z}$  which is typically of the order of  $St$ , and thus small. Caustic formation requires the activation of the non-linear term in Eq. (2) that drives the particle-velocity gradients into a caustic. This in turn, requires rare and violent fluctuations of the fluid-velocity gradients  $\mathbb{A}$  of the order of unity.

We determine the dominant events that drive caustic formation by measuring the statistics of paths in the joint space of  $\mathcal{Z}$  and the fluid velocity gradients  $\mathbb{A}$ . In isotropic turbulence, the properties of any statistical quantity must be invariant under rotations. In addition to  $\mathcal{Z}$ , we therefore map out the paths of the invariants obtained from the symmetric ( $\mathbb{S}$ ) and anti-symmetric ( $\mathbb{O}$ ) parts of the fluid-velocity gradient matrix  $\mathbb{A}$ :  $\omega^2 = \text{Tr} \mathbb{O} \mathbb{O}^T$  and  $\sigma^2 = \text{Tr} \mathbb{S} \mathbb{S}^T$ . Figure 2 shows the paths to caustic formation obtained by numerical simulation, using

DNS of two-dimensional incompressible turbulence (simulation details in Supplemental Material [33]). The path density is colour-coded with the highest densities shown in yellow.

Panel (a) shows paths to caustic formation in the  $Z$  -  $\mathcal{A}^2$ -plane, where  $\mathcal{A}^2 = \omega^2 - \sigma^2 = \text{Tr}(\mathbb{A}^2)$ . We see that most paths (yellow regions) that reach a caustic at  $Z = -\infty$  pass a large fluid-gradient threshold  $\mathcal{A}^2 \approx 0.2$ . The dashed line shows the dynamics obtained in perturbation theory [26],  $Z \sim -\mathcal{A}^2$ , conventionally used to describe the effect of preferential concentration [27]. Note that the perturbative approximation fails to describe caustic formation because it predicts that  $\mathcal{Z}$  stays finite. The solid line describes the result of a stability analysis. It ends in a bifurcation point that initiates caustic formation (see below).

Panel (b) shows that typical paths to caustic formation correspond to large strain  $\sigma^2$ . Vorticity  $\omega^2$ , by contrast, remains small for the majority of paths. Panel (c) shows the time evolution of  $\sigma^2$  and  $\omega^2$  prior to caustic formation at  $t = 0$ . We observe that while  $\omega^2$  remains small,  $\sigma^2$  increases sharply, reaches a large value, and then decreases again until the caustic is formed. The majority of the large strain persist until the caustic is formed, suggesting that caustics preferentially form in regions of large strain. Appealing to optimal-fluctuation theory, our numerical results point towards an optimal path that underlies caustic formation, characterised by small vorticity, and a violent strain. Although the spread in our data is quite large at the value of the Stokes number we used,  $St = 0.31$ , the optimal path leaves a strong mark in our data, reflected by the yellow streaks in Fig. 2.

We explain our observations using an optimal fluctuation approach. The first step is to analyse the fixed-point structure and the bifurcations of Eq. (2). We expand the equation of motion (2) for the  $2 \times 2$  matrix  $\mathbb{Z}$  in a basis of matrices generated by the identity matrix  $\mathbb{I}$  and

$$\mathbf{e}_1 = \begin{pmatrix} 0 & -1 \\ 1 & 0 \end{pmatrix}, \quad \mathbf{e}_2 = \begin{pmatrix} 0 & 1 \\ 1 & 0 \end{pmatrix}, \quad \mathbf{e}_3 = \begin{pmatrix} 1 & 0 \\ 0 & -1 \end{pmatrix}. \quad (4)$$

This basis is orthogonal with respect to the inner product

defined for two matrices  $\mathbb{M}$  and  $\mathbb{N}$  by  $\langle \mathbb{M}, \mathbb{N} \rangle = \frac{1}{2} \text{Tr}[\mathbb{M}\mathbb{N}]$ , so that  $\langle \mathbf{e}_i, \mathbf{e}_j \rangle = g_{ij} = g^{ij} = \text{diag}(-1, 1, 1)_{ij}$  and  $\mathbf{e}_i^\top = \mathbf{e}^i = g^{ij} \mathbf{e}_j$ . We call  $z^i(t) \equiv \langle \mathbf{e}^i, \mathbb{Z}(t) \rangle$  and  $A^i(t) \equiv \langle \mathbf{e}^i, \mathbb{A}(t) \rangle$ . This formulation in terms of the Lorentzian metric  $g_{ij}$  [34] is convenient, because it disentangles the strain and vorticity parts of the fluid-velocity gradients  $\mathbb{A}$ . We have  $\mathbb{O} = \omega \mathbf{e}_1$ , so that  $A^1 = \omega$  describes the vorticity. The other components,  $A^2$  and  $A^3$ , describe the strain,  $\mathbb{S} = A^2 \mathbf{e}_2 + A^3 \mathbf{e}_3$ . Similarity transformations of  $\mathbb{Z}$ ,  $\tilde{\mathbb{Z}} = \mathbb{P}\mathbb{Z}\mathbb{P}^{-1}$ , leave  $\mathbb{Z}$  invariant, but transform  $z^i$  by means of a proper Lorentz transformation  $\tilde{z}^i = \Lambda_j^i z^j$ . The same holds for transformations of  $\mathbb{A}$ . The matrix  $\Lambda$  which transforms the three-vectors  $A^i$  and  $z^i$  has the properties  $\Lambda^\top g \Lambda = g$ , and  $\det \Lambda = 1$ .

Expanding Eq. (2) in the basis (4) we obtain,

$$\text{St} \frac{d}{dt} \mathbb{Z} = -\mathbb{Z} - \frac{1}{2} \mathbb{Z}^2 - 2z_i z^i, \quad (5a)$$

$$\text{St} \frac{d}{dt} z^i = -(\mathbb{Z} + 1) z^i + A^i. \quad (5b)$$

As the time-derivatives on the left-hand side of Eq. (5) are multiplied by  $\text{St} \ll 1$ , we expect the dynamics of  $\mathbb{Z}$  and  $z^i$  to take place in the vicinity of its stable fixed points, if they exist. For  $A^i = 0$  we find three fixed points,  $\mathbb{Z} = z^i = 0$ ,  $\mathbb{Z} = -2, z^i = 0$  and  $\mathbb{Z} = -1, z_i z^i = 1/4$ , whose stability is determined by the eigenvalues of the stability matrix of (5). The fixed point  $\mathbb{Z} = z^i = 0$  is stable for  $A^i = 0$ , but a bifurcation occurs at finite  $A^i$ ,  $(\mathbb{Z}, \mathcal{A}^2) = (-1 + 1/\sqrt{2}, 1/8)$ , where the fixed point disappears. We conclude that when  $\mathcal{A}^2 < 1/8$  the dynamics (5) takes place in the vicinity of the stable fixed point obtained from the implicit equation

$$-\mathbb{Z}(\mathbb{Z}/2 + 1)(\mathbb{Z} + 1)^2 \sim \mathcal{A}^2 = \sigma^2 - \omega^2. \quad (6)$$

When  $\mathcal{A}^2$  exceeds  $1/8$  the fixed point ceases to exist, and the nonlinear dynamics (5) drives  $\mathbb{Z}$  to negative infinity, forming a caustic. The evolution (6) of the stable fixed point as a function of  $\mathcal{A}^2$  and  $\sigma^2$  is shown as the solid lines in Figs. 2(a) and (b) which end at the bifurcation point,  $(-1 + 1/\sqrt{2}, 1/8)$ , (black dot). Hence, for  $\mathcal{A}^2 < 1/8$  particle neighbourhoods are stable and are continuously deformed by the fluid-velocity gradients, according to Eq. (6). For  $\mathcal{A}^2 > 1/8$ , however, the neighbourhoods become unstable, and collapse after a short time. Expanding Eq. (6) for small  $\mathbb{Z}$ , we recover the perturbative approximation [26],  $\mathbb{Z} \sim -\mathcal{A}^2$ , which incorrectly predicts that particle neighbourhoods are always stable.

Our stability analysis of Eq. (5) explains the qualitative shape of the paths in Fig. 2(a). However, it misses some of the important results of our DNS. In particular, the stability analysis does not explain why only the strain contributes to caustic formation and vorticity remains small [Fig. 2(b)], and it has no bearing on the time-evolution of the large gradient fluctuations shown in Figs. 2(c). Finally, it does not account for the observation that the threshold reached by most paths is actually slightly larger than  $1/8 = 0.125$ .

In order to explain these parts of our observations we need to go beyond the stability analysis, and consider how the fluid-velocity gradients reach the large threshold required to render particle neighbourhoods unstable. We do this in the following by computing their optimal fluctuation.

The correlation functions of  $\mathbb{S}$  and  $\mathbb{O}$ , evaluated along particle trajectories in isotropic and homogeneous turbulence, have the general form

$$\langle S_{ik}(t) S_{jl}(t') \rangle = C_{ijkl}^S \langle \text{Tr} \mathbb{S}(t) \mathbb{S}^\top(t') \rangle, \quad (7a)$$

$$\langle O_{ik}(t) O_{jl}(t') \rangle = C_{ijkl}^O \langle \text{Tr} \mathbb{O}(t) \mathbb{O}^\top(t') \rangle, \quad (7b)$$

and  $\langle S_{ik}(t) O_{jl}(t') \rangle = 0$ . In two spatial dimensions, the tensors in Eqs. (7) are given by  $C_{ijkl}^S = 1/4(\delta_{ij}\delta_{kl} + \delta_{il}\delta_{jk} - \delta_{ik}\delta_{jl})$  and  $C_{ijkl}^O = 1/2(\delta_{ij}\delta_{kl} - \delta_{il}\delta_{jk})$ . We express Eq. (7) in terms of the basis (4) to obtain the correlations of  $A^i$ ,

$$\langle A^1(t) A^1(t') \rangle = \frac{1}{2} \langle \text{Tr} \mathbb{O}(t) \mathbb{O}^\top(t') \rangle, \quad (8)$$

$$\langle A^2(t) A^2(t') \rangle = \langle A^3(t) A^3(t') \rangle = \frac{1}{4} \langle \text{Tr} \mathbb{S}(t) \mathbb{S}^\top(t') \rangle.$$

All other correlations of  $A^i$  are zero. The right-hand sides of Eqs. (8) are parametrised as

$$\langle \text{Tr} \mathbb{S}(t) \mathbb{S}^\top(t') \rangle = \text{St}^2 C_S(\text{St}) f(|t - t'|/s), \quad (9a)$$

$$\langle \text{Tr} \mathbb{O}(t) \mathbb{O}^\top(t') \rangle = \text{St}^2 C_O(\text{St}) g(|t - t'|/o), \quad (9b)$$

with the non-dimensional correlation times  $s$  and  $o$  of  $\mathbb{S}$  and  $\mathbb{O}$ , respectively. For tracer particles with  $\text{St} = 0$  one has  $C_S(0) = C_O(0) = 1/2$ . Inertial particles with  $\text{St} > 0$  tend to avoid vortical regions due to preferential concentration [26, 27], so that  $C_O(\text{St}) < 1/2$ . The amplitude  $C_S$ , on the other hand, remains approximately equal to  $1/2$  [23]. In our two-dimensional numerics we also find  $C_S(\text{St}) \approx 1/2$ , for Stokes numbers between 0.21 and 0.51. The functions  $f$  and  $g$  in Eqs. (9) are normalised to unity,  $f(0) = g(0) = 1$ . Their time dependences are well approximated by exponential functions for  $|t - t'| > s, o$ . We therefore model the gradient processes  $A^i$  by independent Ornstein-Uhlenbeck processes [35] with increments

$$dA^i = -\gamma^i A dt + \varepsilon^i dW_t^i, \quad (10)$$

where  $\gamma^1 = \sigma^{-1}$ ,  $\gamma^2 = \gamma^3 = s^{-1}$  and  $\varepsilon^1 = \text{St} C_O(\text{St})^{1/2} \sigma^{-1/2}$ ,  $\varepsilon^2 = \varepsilon^3 = \text{St} C_S(\text{St})^{1/2} (2s)^{-1/2}$ . This way, they have the correlations given in Eqs. (7) and (9), with  $f(t) = g(t) = e^{-t}$ . For Ornstein-Uhlenbeck processes the most probable (optimal) fluctuation  $A_{\text{opt}}^i$  reaching a given threshold, is readily obtained by optimal-fluctuation methods [36]. The optimal path that starts at a typical configuration of  $A^i$  at time  $t_0$ , and that reaches a threshold value  $\mathcal{A}_{\text{th}}^2 = 2A(t_{\text{th}})_i A(t_{\text{th}})_i$  at a given time  $t_{\text{th}}$ , is given by  $A_{\text{opt}}^1 = a^1 e^{-|t - t_{\text{th}}|/o}$  and  $A_{\text{opt}}^{2,3} = a^{2,3} e^{-|t - t_{\text{th}}|/s}$  with  $2a_i a^i = \mathcal{A}_{\text{th}}^2$ . The individual parameters  $a^i$  are obtained by minimising the action  $S$

$$S = \frac{1}{\text{St}^2} \left( \frac{a_1^2}{C_O(\text{St})} + \frac{2(a_2^2 + a_3^2)}{C_S(\text{St})} \right), \quad (11)$$

over all  $a_1$ ,  $a_2$  and  $a_3$  subject to the constraint  $2a_i a^i = \mathcal{A}_{\text{th}}^2$ . We find  $a_1 = 0$ ,  $2(a_2^2 + a_3^2) = \mathcal{A}_{\text{th}}^2$  with minimal action  $S = \mathcal{A}_{\text{th}}^2 / [\text{St}^2 C_S(\text{St})]$ . In other words, the optimal fluctuation of the fluid-velocity gradients is free of vorticity,  $\omega_{\text{opt}}^2 = 2a_1^2 = 0$ , in agreement with our DNS in Figs. 2(b) and (c). This result is intuitive: Vorticity contributes to  $\mathcal{A}^2$  with a negative sign, so that any fluctuation of  $\mathcal{A}^2 = \sigma^2 - \omega^2$  that reaches the large threshold  $\mathcal{A}_{\text{th}}^2$  with finite vorticity, requires an even larger strain contribution, to make up for vorticity. The optimal way to reach the threshold value is thus through paths that are vorticity-free. By contrast, the strain grows exponentially as  $\sigma_{\text{opt}}^2 = \mathcal{A}_{\text{th}}^2 e^{-2|t-t_{\text{th}}|/s}$  for  $t < t_{\text{th}}$ . After the strain has reached the threshold at  $t_{\text{th}}$ , it decreases. Additional details of our calculations are given in the Supplemental Material [33].

Using the optimal gradient fluctuation, we now obtain the explicit form for the optimal path  $(\mathcal{Z}_{\text{opt}}, \sigma_{\text{opt}}^2)$  as a function of time. For  $\text{St} \ll 1$ , the left-hand sides of Eqs. (5) are small most of the time. To evaluate  $\mathcal{Z}_{\text{opt}}$  we therefore use  $A_{\text{opt}}^i$  as an input into Eq. (5). Making use of the fact that the vorticity is zero along the optimal path,  $\omega_{\text{opt}} = 0$ , we find that  $A_{\text{opt}} = A_{\text{opt}}^i e_i$  and  $\mathcal{Z}_{\text{opt}} = 1/2 \mathcal{Z}_{\text{opt}} + z_{\text{opt}}^i e_i$  can be brought into diagonal form by a Lorentz transformation. The equations for the diagonal entries (eigenvalues)  $\lambda_{\text{opt}}^\pm$  decouple into two equations which are solved individually,

$$\text{St} \frac{d}{dt} \lambda_{\text{opt}}^\pm = -\lambda_{\text{opt}}^\pm - (\lambda_{\text{opt}}^\pm)^2 \pm \frac{\mathcal{A}_{\text{th}}}{\sqrt{2}} e^{-|t-t_{\text{th}}|/s}, \quad (12)$$

with initial conditions  $\lambda^\pm(t_0) = \pm \mathcal{A}_{\text{th}} e^{-|t_0-t_{\text{th}}|/s} / \sqrt{2}$ . The solutions to Eq. (12) can be obtained analytically in terms of Bessel functions, as shown in the Supplemental Material [33]. After solving (12) the optimal path  $\mathcal{Z}_{\text{opt}}$  is obtained by  $\mathcal{Z}_{\text{opt}} = \lambda_{\text{opt}}^+ + \lambda_{\text{opt}}^-$ .

We note that, for finite  $\text{St}$ , the threshold value  $\mathcal{A}_{\text{th}}^2$  exceeds the value  $1/8$  obtained from the stability analysis, in agreement with our DNS. The reason is that the optimal strain fluctuation  $\sigma_{\text{opt}}^2(t)$  decreases for  $t > t_{\text{th}}$ . In order for  $\mathcal{Z}_{\text{opt}}$  to reach negative infinity,  $\sigma_{\text{opt}}^2(t)$  must exceed  $1/8$  for a finite time, in order to enable  $\mathcal{Z}_{\text{opt}}$  to become large and negative. The time for which the threshold must exceed  $1/8$  decreases as  $\text{St}$  becomes smaller, and we recover  $\mathcal{A}^2 \rightarrow 1/8$  in the limit  $\text{St} \rightarrow 0$ .

In Fig. 3 we compare our theory and DNS. The dashed line in Fig. 3(a) shows  $(\mathcal{Z}_{\text{opt}}, \sigma_{\text{opt}}^2)$  obtained from Eqs. (12), with  $\text{St} = 0.31$  and dimensionless correlation time  $s = 2.4$ , determined numerically. We observe qualitative agreement between the theoretically obtained optimal path and the (yellow) regions of high path density. However, Eqs. (12) over-estimate the threshold value  $\mathcal{A}_{\text{th}}^2$  by a factor of about 2. The likely reason is that the Stokes number in our DNS is too large to closely follow our analytical results, valid for  $\text{St} \ll 1$ . Quantitative agreement between theory and DNS is achieved by using a slightly smaller Stokes number,  $\text{St} = 0.15$ , in Eqs. (12) [solid line in Fig. 3(a)].

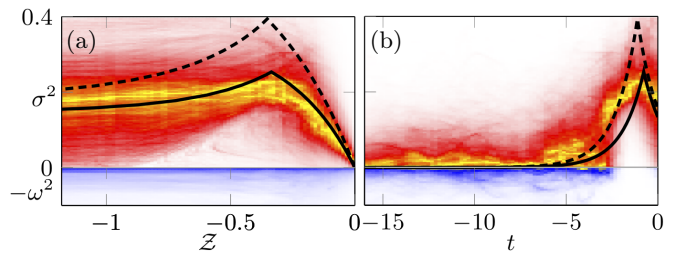


FIG. 3. Optimal paths obtained from theory and path density for  $\text{St} = 0.31$  from DNS. (a)  $(\mathcal{Z}_{\text{opt}}, \sigma_{\text{opt}}^2)$  from theory for  $\text{St} = 0.31$  (dashed line) and  $\text{St} = 0.15$  (solid line). The color-coded path density is the same as in Fig. 2(b). (b)  $\sigma_{\text{opt}}^2(t)$  from theory for  $\text{St} = 0.31$  (dashed line) and  $0.15$  (solid line). The color-coded path density is the same as in Fig. 2(c).

Figure 3(b) shows  $\sigma_{\text{opt}}^2(t)$  obtained from theory with  $\text{St} = 0.31$  (dashed line) and the corresponding path density from our DNS. Again, reducing the Stokes number in our theory to  $\text{St} = 0.15$  achieves a better approximation of the data. The theory correctly predicts that a considerable fraction of the large strain required to initialise the caustic persists until it forms at  $t = 0$ . This explains why caustics form mainly in regions of large strain. For other Stokes numbers between 0.24 and 0.51, our DNS results lead to the same conclusion (data not shown).

In conclusion, we explained caustic formation in turbulent aerosols at small particle inertia as an optimal-fluctuation problem. In order for caustics to form, the fluid-velocity gradients must follow an optimal path, characterised by small vorticity and a violent strain that exceeds a large threshold. The remnants of the optimal fluctuation at the time of caustic formation result in a strong instantaneous correlation between large strains and caustic events.

Since caustics give rise to a multivalued particle-velocity field, and thus to high relative particle velocities, our results provide an explanation for the recently observed, instantaneous correlation between particle collisions and intense strain [23, 24]. The characteristic shape of the optimal path to caustic formation will allow to identify caustics in experiments, and the strong instantaneous correlation of caustics and strain makes it possible to efficiently sample caustics in simulations.

The stability analysis described in this Letter can be generalised to three dimensions where it reveals that particle neighbourhoods become unstable when the two invariants  $Q = -\text{Tr}A^2/2$  and  $R = -\text{Tr}A^3/3$  reach large thresholds in the  $Q$ - $R$  plane. We therefore speculate that optimal-fluctuation methods also explain caustic formation in three-dimensional turbulence at small Stokes numbers.

## ACKNOWLEDGMENTS

KG thanks J. Vollmer for discussions regarding the role of the invariants  $Q$  and  $R$  for caustic formation in

turbulence. JM, KG, and BM were supported by the grant *Bottlenecks for particle growth in turbulent aerosols* from the Knut and Alice Wallenberg Foundation, Dnr. KAW 2014.0048, and in part by VR grant no. 2017-3865. DM acknowledges the support of the Swedish Research Council Grant No. 638-2013-9243 as well as 2016-05225. VP and PP acknowledge support from intramu-

ral funds at TIFR Hyderabad from the Department of Atomic Energy (DAE), India and DST (India) Project No. ECR/2018/001135. The simulations were performed on resources provided by the Swedish National Infrastructure for Computing (SNIC) at PDC center for high performance computing.

- 
- [1] Gregory Falkovich, Krzysztof Gawedzki, and Massimo Vergassola, “Particles and fields in fluid turbulence,” *Rev. Mod. Phys.* **73**, 913–975 (2001).
- [2] E. Balkovsky, G. Falkovich, and A. Fouxon, “Intermittent distribution of inertial particles in turbulent flows,” *Phys. Rev. Lett.* **86**, 2790–2793 (2001).
- [3] Jérémie Bec, Luca Biferale, Guido Boffetta, Massimo Cencini, Stefano Musacchio, and Federico Toschi, “Lyapunov exponents of heavy particles in turbulence,” *Phys. Fluids* **18**, 091702 (2006), arXiv:0606024 [nlin].
- [4] K. Gustavsson and B. Mehlig, “Statistical models for spatial patterns of heavy particles in turbulence,” *Adv. Phys.* **65**, 1–57 (2016), arXiv:1412.4374.
- [5] Bernhard Mehlig and Michael Wilkinson, “Coagulation by random velocity fields as a Kramers problem,” *Phys. Rev. Lett.* **92**, 250602 (2004), arXiv:0310603 [cond-mat].
- [6] M. Wilkinson and B. Mehlig, “Caustics in turbulent aerosols,” *Europhys. Lett.* **71**, 186–192 (2005), arXiv:0403011 [cond-mat].
- [7] Michael Wilkinson, Bernhard Mehlig, and Vlad Bezuglyy, “Caustic activation of rain showers,” *Phys. Rev. Lett.* **97**, 048501 (2006), arXiv:0604166 [cond-mat].
- [8] G. Falkovich, A. Fouxon, and M. Stepanov, “Acceleration of rain initiation by cloud turbulence,” *Nature* **419**, 151 (2002).
- [9] G Falkovich and A Pumir, “Sling Effect in Collisions of Water Droplets in Turbulent Clouds,” *J. Atmos. Sci.* **64**, 4497–4505 (2007).
- [10] K. Gustavsson and B. Mehlig, “Distribution of relative velocities in turbulent aerosols,” *Phys. Rev. E* **84**, 045304 (2011), arXiv:1012.1789.
- [11] K. Gustavsson and B. Mehlig, “Relative velocities of inertial particles in turbulent aerosols,” *J. Turbul.* **15**, 34–69 (2014), arXiv:1307.0462.
- [12] V Perrin and H Jonker, “Relative velocity distribution of inertial particles in turbulence - a numerical study,” *Phys. Rev. E* **92**, 043022 (2015).
- [13] Akshay Bhatnagar, K Gustavsson, and Dhruvaditya Mitra, “Statistics of the relative velocity of particles in turbulent flows: Monodisperse particles,” *Phys. Rev. E* **97**, 23105 (2018).
- [14] S. Sundaram and L. R. Collins, “Collision statistics in an isotropic particle-laden turbulent suspension,” *J. Fluid Mech.* **335**, 75–109 (1997).
- [15] M Vořkuhle, A Pumir, E Lévêque, and M Wilkinson, “Prevalence of the sling effect for enhancing collision rates in turbulent suspensions,” *J. Fluid Mech.* **749**, 841 (2014).
- [16] Alain Pumir and Michael Wilkinson, “Collisional aggregation due to turbulence,” *Annu. Rev. Condens. Matter Phys.* **7**, 141–170 (2016).
- [17] Andrea Crisanti, Massimo Falcioni, Antonello Provenzale, Paolo Tanga, and Angelo Vulpiani, “Dynamics of passively advected impurities in simple two-dimensional flow models,” *Phys. Fluids A Fluid Dyn.* **4**, 1805–1820 (1992).
- [18] J E Martin and E Meiburg, “The accumulation and dispersion of heavy particles in forced two-dimensional mixing layers. I. The fundamental and subharmonic cases,” *Phys. Fluids* **6**, 1116–1132 (1994).
- [19] J. Bec, A. Celani, M. Cencini, and S. Musacchio, “Clustering and collisions of heavy particles in random smooth flows,” *Phys. Fluids* **17**, 073301 (2005).
- [20] Lauris Ducasse and Alain Pumir, “Inertial particle collisions in turbulent synthetic flows: quantifying the sling effect,” *Phys. Rev. E* **80**, 66312 (2009).
- [21] K Gustavsson and B Mehlig, “Distribution of velocity gradients and rate of caustic formation in turbulent aerosols at finite Kubo numbers,” *Phys. Rev. E* **87**, 023016 (2013).
- [22] Michael W Reeks, “Transport, mixing and agglomeration of particles in turbulent flows,” *Flow, Turbul. Combust.* **92**, 3–25 (2014).
- [23] Vincent E Perrin and Harm J J Jonker, “Preferred location of droplet collisions in turbulent flows,” *Phys. Rev. E* **89**, 33005 (2014).
- [24] Jason R Picardo, Lokahith Agasthya, Rama Govindarajan, and Samridhi Sankar Ray, “Flow structures govern particle collisions in turbulence,” *Phys. Rev. Fluids* **4**, 32601 (2019).
- [25] Gregory P. Bewley, Ewe Wei Saw, and Eberhard Bodenschatz, “Observation of the sling effect,” *New J. Phys.* **15**, 083051 (2013), arXiv:1312.2901.
- [26] M R Maxey, “The gravitational settling of aerosol particles in homogeneous turbulence and random flow fields,” *J. Fluid Mech.* **174**, 441–465 (1987).
- [27] Kyle D. Squires and John K. Eaton, “Preferential concentration of particles by turbulence,” *Phys. Fluids A* **3**, 1169–1178 (1991).
- [28] J Zittartz and J S Langer, “Theory of bound states in a random potential,” *Phys. Rev.* **148**, 741 (1966).
- [29] A Eriksson, F Elías-Wolff, and B Mehlig, “Metapopulation dynamics on the brink of extinction,” *Theor. Popul. Biol.* **83**, 101–122 (2013).
- [30] Alex Kamenev, Baruch Meerson, and Boris Shklovskii, “How colored environmental noise affects population extinction,” *Phys. Rev. Lett.* **101**, 268103 (2008).
- [31] Victor Gurarie and Alexander Migdal, “Instantons in the Burgers equation,” *Phys. Rev. E* **54**, 4908 (1996).
- [32] Jérémie Bec and Konstantin Khanin, “Burgers turbulence,” *Phys. Rep.* **447**, 1–66 (2007).
- [33] Supplemental Material available at ... which also contains Refs. [37–39].
- [34] Katsumi Nomizu and Ulrich Pinkall, “Lorentzian geome-

- try for 2x2 real matrices,” *Linear Multilinear Algebr.* **28**, 207–212 (1991).
- [35] A Pumir and M Wilkinson, “Orientation statistics of small particles in turbulence,” *New J. Phys.* **13**, 1–18 (2011).
- [36] Tobias Grafke, Rainer Grauer, and Tobias Schäfer, “The instanton method and its numerical implementation in fluid mechanics,” *J. Phys. A Math. Theor.* **48**, 333001 (2015).
- [37] Lars Onsager and Stefan Machlup, “Fluctuations and irreversible processes,” *Phys. Rev.* **91**, 1505 (1953).
- [38] Paul Cecil Martin, E D Siggia, and H A Rose, “Statistical dynamics of classical systems,” *Phys. Rev. A* **8**, 423 (1973).
- [39] R Graham and T Tél, “Existence of a potential for dissipative dynamical systems,” *Phys. Rev. Lett.* **52**, 9 (1984).

# Supplemental material for ‘Paths to caustic formation in turbulent aerosols’

Jan Meibohm,<sup>1</sup> Vikash Pandey,<sup>2</sup> Akshay Bhatnagar,<sup>3</sup> Kristian  
Gustavsson,<sup>1</sup> Dhruvaditya Mitra,<sup>3</sup> Prasad Perlekar,<sup>2</sup> and B. Mehlig<sup>1</sup>

<sup>1</sup>*Department of Physics, Gothenburg University, SE-41296 Gothenburg, Sweden*

<sup>2</sup>*TIFR Centre for Interdisciplinary Sciences, Tata Institute of Fundamental Research, Gopanpally, Hyderabad 500046, India*

<sup>3</sup>*NORDITA, Royal Institute of Technology and Stockholm University,  
Roslagstullsbacken 23, SE-10691 Stockholm, Sweden*

In this supplemental material we provide additional details regarding the analytical calculations summarised in the main text, and for the numerical simulations used to obtain the results shown in Figs. 2 and 3 in the main text.

## I. INSTANTON CALCULATION FOR THE FLUID-VELOCITY GRADIENTS

In this section we explain in detail the instanton calculation outlined in the main text. We consider the problem of the gradient process  $A^i$  reaching a threshold value given by  $2A_i A^i = 2(-A_1^2 + A_2^2 + A_3^2) = \mathcal{A}_{\text{th}}$ . In particular, we explain how to derive Eq. (10), and the time dependence of the optimal path  $A_{\text{opt}}^i(t)$  of the gradient process.

We model the individual components  $A^i$  of the fluid-velocity gradient matrix  $\mathbb{A}$  as independent Ornstein-Uhlenbeck processes with increments [see Eq. (9) in the main text]

$$dA^i(t) = -\gamma^i A(t)dt + \varepsilon^i dW_t^i, \quad (\text{S1})$$

where  $\gamma^1 = o^{-1}$ ,  $\gamma^2 = \gamma^3 = s^{-1}$  and  $\varepsilon^1 = \text{St}C_{\text{O}}(\text{St})^{1/2}o^{-1/2}$ ,  $\varepsilon^2 = \varepsilon^3 = \text{St}C_{\text{S}}(\text{St})^{1/2}(2s)^{-1/2}$ . This notation is explained in the main text. The terms  $dW_t^i$  are independent Brownian increments with zero mean and variance  $dt$ . We consider the transition probability of the gradients  $A^i$  from an initial value, sampled from the equilibrium distribution  $\varrho_{\text{eq}}(A^i(t_0) = \alpha^i)$  at time  $t_0$ , to a large threshold value  $a^i$  at time  $t_{\text{th}}$ . Because the Ornstein-Uhlenbeck processes are independent, we compute this transition probability for a single Ornstein-Uhlenbeck process,

$$dA(t) = -\gamma A(t)dt + \varepsilon dW_t, \quad (\text{S2})$$

and adjust the parameters  $\gamma$  and  $\varepsilon$  in the end, according to the values given above. How to compute the optimal path for an Ornstein-Uhlenbeck process to reach a threshold is well known [1]. We adapted the method to our specific problem, where the process is sampled from the equilibrium distribution at the initial time  $t_0$ . The transition probability of the process (S2) from a value  $\alpha$  sampled from the equilibrium distribution at time  $t_0$ , to  $a$  at time  $t_{\text{th}}$  is written as

$$P(a, t_{\text{th}}, t_0) = \int_{-\infty}^{\infty} d\alpha P\left(A(t_{\text{th}}) = a, t_{\text{th}} \middle| A(t_0) = \alpha, t_0\right) \varrho_{\text{eq}}(A(t_0) = \alpha), \quad (\text{S3})$$

where the equilibrium distribution  $\varrho_{\text{eq}}$  of the Ornstein-Uhlenbeck process reads

$$\varrho_{\text{eq}}(A(t_0) = \alpha) = \sqrt{\frac{\gamma}{\pi\varepsilon^2}} \exp\left(-\frac{\gamma\alpha^2}{\varepsilon^2}\right) = \mathcal{N}_0 \exp\left(-\frac{S_0(\alpha)}{\varepsilon^2}\right), \quad (\text{S4})$$

with  $S_0(\alpha) = \gamma\alpha^2$  and normalisation factor  $\mathcal{N}_0$ . The transition probability  $P(A_{t_{\text{th}}} = a, t_{\text{th}} | A_{t_0} = \alpha, t_0)$  can be written in terms of a path integral

$$P(A_{t_{\text{th}}} = a, t_{\text{th}} | A_{t_0} = \alpha, t_0) = \mathcal{N} \int_{A(t_0)=\alpha}^{A(t_{\text{th}})=a} \mathcal{D}A(t) \exp\left(-\frac{S[A]}{\varepsilon^2}\right), \quad (\text{S5})$$

an integral over paths starting at  $A(t_0) = \alpha$  and ending at  $A(t_{\text{th}}) = a$ . In Eq. (S5),  $\mathcal{N}$  is a normalisation factor, and the action  $S[A]$  is given by

$$S[A] = \int_{t_0}^{t_{\text{th}}} dt \frac{1}{2} \left( \frac{d}{dt} A(t) + \gamma A(t) \right)^2 = \int_{t_0}^{t_{\text{th}}} dt \mathcal{L}[A, \frac{d}{dt} A]. \quad (\text{S6})$$

The last equality defines the Onsager-Machlup Lagrangian  $\mathcal{L}$  [2]. We write Eq. (S3) as

$$P(a, t_{\text{th}}, t_0) = \mathcal{N} \mathcal{N}_0 \int_{-\infty}^{\infty} d\alpha \int \mathcal{D}A(t) \exp\left(-\frac{S[A]}{\varepsilon^2} - \frac{S_0(\alpha)}{\varepsilon^2}\right). \quad (\text{S7})$$

We consider weak-inertia case  $\text{St} \ll 1$  which corresponds to  $\varepsilon \ll 1$ . In this case, the path integration in Eq. (S7) is well-known to concentrate around an ‘optimal path’  $A_{\text{opt}}(t)$ . This path is obtained by a variation of the action  $S[A] + S_0(\alpha)$  over histories of  $A(t)$ . This variation must vanish at the optimal path:

$$0 = \delta S[A] + \delta A(t_0) \frac{d}{d\alpha} S_0(\alpha)|_{\alpha=A(t_0)} = -\delta A(t_0) \left( \frac{d}{dt} A(t_0) + \gamma A(t_0) \right) + \delta A(t_0) 2\gamma A(t_0) + \int_{t_0}^{t_{\text{th}}} dt \delta A \left( \frac{d}{dt} \frac{\partial \mathcal{L}[A, \frac{d}{dt} A]}{\partial \frac{d}{dt} A} - \frac{\partial \mathcal{L}[A, \frac{d}{dt} A]}{\partial A} \right). \quad (\text{S8})$$

The argument of the integral is the Euler-Lagrange equation which determines the optimal path  $A_{\text{opt}}$ . The first term is a boundary term, the second term comes from the variation of the equilibrium distribution. Another boundary

term at time  $t_{\text{th}}$  vanishes, because the variation  $\delta A(t_{\text{th}})$  must be zero, as the end points of all trajectories are fixed to  $A(t_{\text{th}}) = a$ . Combining the first two terms in Eq. (S8) one obtains the boundary conditions

$$\frac{d}{dt}A_{\text{opt}}(t_0) - \gamma A_{\text{opt}}(t_0) = 0, \quad A_{\text{opt}}(t_{\text{th}}) = a. \quad (\text{S9})$$

It is convenient to move to a Hamiltonian formulation [3, 4] in terms of the Hamiltonian  $\mathcal{H}$  given by

$$\mathcal{H} = p_{\text{opt}} \frac{d}{dt}A_{\text{opt}} - \mathcal{L} = \frac{p_{\text{opt}}^2}{2} (p_{\text{opt}} - 2\gamma A_{\text{opt}}) = E, \quad (\text{S10})$$

where  $p = \partial \mathcal{L} / \partial (\frac{d}{dt}A_{\text{opt}}) = \frac{d}{dt}A_{\text{opt}} + \gamma A_{\text{opt}}$  is the momentum conjugate to  $A$ , and  $E$  is a constant of motion. The initial condition in Eq. (S9) is expressed in terms of  $p_{\text{opt}}$  as  $p_{\text{opt}}(t_0) - 2\gamma A_{\text{opt}}(t_0) = 0$ . This allows to determine  $E$  as  $E = 0$ . From Eq. (S10) we then find

$$p_{\text{opt}}(t) = 2\gamma A_{\text{opt}}(t), \quad (\text{S11})$$

for  $t \leq t_{\text{th}}$ . For  $t > t_{\text{th}}$ , the motion is unconstrained and behaves classically, so that

$$p_{\text{opt}}(t) = 0. \quad (\text{S12})$$

In the Hamiltonian formulation, the equations of motion equivalent to the Euler-Lagrange equations are the Hamiltonian equations of motion

$$\frac{d}{dt}A_{\text{opt}} = p_{\text{opt}} - \gamma A_{\text{opt}}, \quad \frac{d}{dt}p_{\text{opt}} = \gamma p_{\text{opt}}. \quad (\text{S13})$$

Combining Eqs. (S13) with Eqs. (S11) and (S12) we obtain

$$\frac{d}{dt}A_{\text{opt}}(t) = \gamma A_{\text{opt}}(t), \quad t \leq t_{\text{th}}, \quad (\text{S14})$$

$$\frac{d}{dt}A_{\text{opt}}(t) = -\gamma A_{\text{opt}}(t), \quad t > t_{\text{th}}, \quad (\text{S15})$$

with solution

$$A_{\text{opt}}(t) = ae^{-\gamma|t-t_{\text{th}}|}. \quad (\text{S16})$$

The exponential scaling of the transition probability (S7) is obtained to leading order in  $\varepsilon$  from the saddle point approximation

$$P(a, t_{\text{th}}, t_0) \propto \exp \left[ -\frac{S[A_{\text{opt}}]}{\varepsilon^2} - \frac{S_0(\alpha)}{\varepsilon^2} \right]. \quad (\text{S17})$$

We write  $S[A_{\text{opt}}] + S_0(\alpha)$  as

$$\begin{aligned} S[A_{\text{opt}}] + S_0[A_{\text{opt}}(t_0)] &= \int_{t_0}^{t_{\text{th}}} dt \frac{p_{\text{opt}}^2}{2} + \gamma \alpha^2 = \int_{\alpha}^a dA_{\text{opt}} p_{\text{opt}} + \gamma \alpha^2, \\ &= \gamma(a^2 - \alpha^2) + \gamma \alpha^2 = \gamma a^2. \end{aligned} \quad (\text{S18})$$

We arrive at

$$P(a, t_{\text{th}}, t_0) \propto \exp \left[ -\frac{\gamma a^2}{\varepsilon^2} \right]. \quad (\text{S19})$$

The same result for the action is obtained by starting from a fixed initial point, and letting  $t_0 \rightarrow -\infty$  [1], but the optimal paths are slightly different. The final results, Eqs. (S16) and (S19), valid for any Ornstein-Uhlenbeck process of the form (S2), can now be applied to the specific, independent processes (S1) to obtain our final result

$$A_{\text{opt}}^1 = a^1 e^{-|t-t_{\text{th}}|/o}, \quad A_{\text{opt}}^{2,3} = a^{2,3} e^{-|t-t_{\text{th}}|/s}, \quad (\text{S20})$$

$$P(a^i, t_{\text{th}}, t_0) \propto \exp \left[ -\frac{(a^1)^2}{\text{St}^2 C_O(\text{St})} - \frac{2[(a^2)^2 + (a^3)^2]}{\text{St}^2 C_S(\text{St})} \right]. \quad (\text{S21})$$

Equation (S20) is the optimal path for the gradient process given in the main text. The exponent of Eq. (S21) is Eq. (10) in the main text.

## II. ANALYTICAL SOLUTION TO THE EIGENVALUE EQUATIONS FOR $\mathcal{Z}$

We now show our analytical solutions for the optimal path for  $\mathcal{Z} = \text{Tr}\mathbb{Z} = \lambda^+ + \lambda^-$  for small  $\text{St} \ll 1$  [see main text below Eq. (11)]. We first explain how to derive Eq. (11) in the main text. Then we show how to solve the equation in analytic form.

After minimising the action (S21) over values of  $a^i$  subject to the constraint  $2a_i a^i = \mathcal{A}_{\text{th}}^2$ , we find  $a^1 = 0$  and  $2[(a^2)^2 + (a^3)^2] = \mathcal{A}_{\text{th}}^2$ . We write

$$\text{St} \frac{d}{dt} \mathcal{Z}_{\text{opt}} = -\mathcal{Z}_{\text{opt}} - \frac{1}{2} \mathcal{Z}_{\text{opt}}^2 - 2(z_{\text{opt}})_i z_{\text{opt}}^i, \quad (\text{S22a})$$

$$\text{St} \frac{d}{dt} z_{\text{opt}}^1 = -(\mathcal{Z}_{\text{opt}} + 1) z_{\text{opt}}^1, \quad (\text{S22b})$$

$$\text{St} \frac{d}{dt} z_{\text{opt}}^2 = -(\mathcal{Z}_{\text{opt}} + 1) z_{\text{opt}}^2 + a^2 e^{-|t-t_{\text{th}}|/s}, \quad (\text{S22c})$$

$$\text{St} \frac{d}{dt} z_{\text{opt}}^3 = -(\mathcal{Z}_{\text{opt}} + 1) z_{\text{opt}}^3 + a^3 e^{-|t-t_{\text{th}}|/s}. \quad (\text{S22d})$$

At time  $t = t_0$  we have  $\mathbb{Z}(t_0) = \mathbb{A}(t_0)$ , so that  $\mathcal{Z}_{\text{opt}}(t_0) = 0$ . We conclude that  $z_{\text{opt}}^1(t) = 0$  for all times. Now, we perform a Lorentz transform, which in this case is just a simple rotation, of the remaining components  $A_{\text{opt}}^2$  and  $A_{\text{opt}}^3$  so that  $\tilde{A}_{\text{opt}}^2 = 0$  and  $\tilde{A}_{\text{opt}}^3 = \sqrt{(a^2)^2 + (a^3)^2} e^{-|t-t_{\text{th}}|/s} = \mathcal{A}_{\text{th}} e^{-|t-t_{\text{th}}|/s} / \sqrt{2}$ . This leaves the general form of Eqs. (S22) invariant, so that we obtain after the transform

$$\text{St} \frac{d}{dt} \mathcal{Z}_{\text{opt}} = -\mathcal{Z}_{\text{opt}} - \frac{1}{2} \mathcal{Z}_{\text{opt}}^2 - 2(\tilde{z}_{\text{opt}})_i \tilde{z}_{\text{opt}}^i, \quad (\text{S23a})$$

$$\text{St} \frac{d}{dt} \tilde{z}_{\text{opt}}^2 = -(\mathcal{Z}_{\text{opt}} + 1) \tilde{z}_{\text{opt}}^2, \quad (\text{S23b})$$

$$\text{St} \frac{d}{dt} \tilde{z}_{\text{opt}}^3 = -(\mathcal{Z}_{\text{opt}} + 1) \tilde{z}_{\text{opt}}^3 + \frac{\mathcal{A}_{\text{th}}}{\sqrt{2}} e^{-|t-t_{\text{th}}|/s}. \quad (\text{S23c})$$

From  $\tilde{\mathbb{Z}}(t_0) = \tilde{\mathbb{A}}(t_0)$  we again conclude  $\tilde{z}_{\text{opt}}^2(t) = 0$  for all times. Using the initial decomposition we obtain  $\tilde{\mathbb{Z}}_{\text{opt}} = \mathcal{Z}_{\text{opt}}/2\mathbb{1} + \tilde{z}^3 \mathbf{e}_3$ , where  $\mathbf{e}_3$  is diagonal with elements  $\mathbf{e}_3 = \text{diag}(1, -1)$ . Hence, we find that after the transformation,  $\tilde{\mathbb{Z}}_{\text{opt}}$  is in diagonal form with eigenvalues  $\lambda_{\text{opt}}^+ = \mathcal{Z}_{\text{opt}}/2 + \tilde{z}_{\text{opt}}^3$  and  $\lambda_{\text{opt}}^- = \mathcal{Z}_{\text{opt}}/2 - \tilde{z}_{\text{opt}}^3$ . Taking time-derivatives of these eigenvalues, and using Eqs. (S23), we thus obtain the uncoupled equations for the eigenvalues  $\lambda_{\text{opt}}^+$  and  $\lambda_{\text{opt}}^-$ ,

$$\text{St} \frac{d}{dt} \lambda_{\text{opt}}^+ = -\lambda_{\text{opt}}^+ - (\lambda_{\text{opt}}^+)^2 + \frac{\mathcal{A}_{\text{th}}}{\sqrt{2}} e^{-|t-t_{\text{th}}|/s}, \quad (\text{S24a})$$

$$\text{St} \frac{d}{dt} \lambda_{\text{opt}}^- = -\lambda_{\text{opt}}^- - (\lambda_{\text{opt}}^-)^2 - \frac{\mathcal{A}_{\text{th}}}{\sqrt{2}} e^{-|t-t_{\text{th}}|/s}, \quad (\text{S24b})$$

presented in Eq. (11) in the main text. As the trace of a matrix is just the sum of its eigenvalues, we have  $\mathcal{Z}_{\text{opt}} = \text{Tr}\mathbb{Z}_{\text{opt}} = \lambda_{\text{opt}}^+ + \lambda_{\text{opt}}^-$ . These equations need to be solved with the initial conditions  $\lambda_{\text{opt}}^+(t_0) = \frac{\mathcal{A}_{\text{th}}}{\sqrt{2}} e^{-|t_0-t_{\text{th}}|/s}$  and  $\lambda_{\text{opt}}^-(t_0) = -\frac{\mathcal{A}_{\text{th}}}{\sqrt{2}} e^{-|t_0-t_{\text{th}}|/s}$ . We first rescale time with  $\text{St}$  according to  $t \rightarrow \text{St}t$ ,  $t_{\text{th}} \rightarrow \text{St}t_{\text{th}}$ , to obtain,

$$\frac{d}{dt} \lambda_{\text{opt}}^\pm = -\lambda_{\text{opt}}^\pm - (\lambda_{\text{opt}}^\pm)^2 \pm \frac{\mathcal{A}_{\text{th}}}{\sqrt{2}} e^{-\text{St}|t-t_{\text{th}}|/s}, \quad (\text{S25})$$

with initial conditions  $\lambda_{\text{opt}}^\pm(t_0) = \pm \frac{\mathcal{A}_{\text{th}}}{\sqrt{2}} e^{-\text{St}|t_0-t_{\text{th}}|/s}$ . We now express  $\lambda_{\text{opt}}^\pm$  as  $\lambda_{\text{opt}}^\pm = (e^{-t/2} \nu^\pm)^{-1} \frac{d}{dt} [e^{-t/2} \nu^\pm]$ , with initial conditions  $\frac{d}{dt} \nu^\pm(t_0) = 1/2 \pm \frac{\mathcal{A}_{\text{th}}}{\sqrt{2}} e^{-\text{St}|t_0-t_{\text{th}}|/s}$  and  $\nu^\pm(t_0) = 1$ . The variables  $\nu^\pm(t)$  solve the equations

$$\frac{d^2}{dt^2} \nu^\pm = \left( \frac{1}{4} \pm \frac{\mathcal{A}_{\text{th}}}{\sqrt{2}} e^{-\text{St}|t-t_{\text{th}}|/s} \right) \nu^\pm. \quad (\text{S26})$$

We introduce a rescaled time  $\tilde{t} = \sqrt[4]{2^3} \sqrt{\mathcal{A}_{\text{th}}} e^{-\text{St}|t-t_{\text{th}}|/(2s)} s / \text{St}$ , so that

$$\frac{d^2}{dt^2} = \frac{d\tilde{t}}{dt} \frac{d}{d\tilde{t}} \frac{d\tilde{t}}{dt} \frac{d}{d\tilde{t}} = \left( \frac{\text{St}}{2s} \right)^2 \left( \tilde{t}^2 \frac{d^2}{d\tilde{t}^2} + \tilde{t} \frac{d}{d\tilde{t}} \right), \quad (\text{S27})$$

and

$$\tilde{t}^2 \frac{d^2}{d\tilde{t}^2} \nu^+ + \tilde{t} \frac{d}{d\tilde{t}} \nu^+ - \left( \tilde{t}^2 + \frac{s^2}{\text{St}^2} \right) \nu^+ = 0, \quad (\text{S28a})$$

$$\tilde{t}^2 \frac{d^2}{d\tilde{t}^2} \nu^- + \tilde{t} \frac{d}{d\tilde{t}} \nu^- + \left( \tilde{t}^2 - \frac{s^2}{\text{St}^2} \right) \nu^- = 0. \quad (\text{S28b})$$

These are Bessel differential equations, which are solved by Bessel functions. Due to the different signs in Eqs. (S28), the solution for  $\nu^+$  is given by a linear combination of the modified Bessel functions  $I_{\frac{s}{St}}$  and  $I_{-\frac{s}{St}}$ , while  $\nu^-$  is given by a linear combination of the ordinary Bessel functions  $J_{\frac{s}{St}}$  and  $J_{-\frac{s}{St}}$ . Using these fundamental solutions, and taking into account the boundary conditions described above, one obtains exact solutions for  $\lambda^\pm$ . The final solution for  $\lambda^+$  reads

$$\lambda^+(t) = -\frac{1}{2} + \frac{St}{2s} \hat{t}(t) \times \begin{cases} \frac{I'_{\frac{s}{St}}[\hat{t}(t)] + c^+ I'_{-\frac{s}{St}}[\hat{t}(t)]}{I_{\frac{s}{St}}[\hat{t}(t)] + c^+ I_{-\frac{s}{St}}[\hat{t}(t)]}, & t \leq t_{\text{th}}, \\ -\frac{I'_{\frac{s}{St}}[\hat{t}(t)] + d^+ I'_{-\frac{s}{St}}[\hat{t}(t)]}{I_{\frac{s}{St}}[\hat{t}(t)] + d^+ I_{-\frac{s}{St}}[\hat{t}(t)]}, & t > t_{\text{th}}. \end{cases} \quad (\text{S29})$$

$$= \frac{St}{2s} \hat{t}(t) \times \begin{cases} \frac{I_{\frac{s}{St}+1}[\hat{t}(t)] + c^+ I_{-\frac{s}{St}-1}[\hat{t}(t)]}{I_{\frac{s}{St}}[\hat{t}(t)] + c^+ I_{-\frac{s}{St}}[\hat{t}(t)]}, & t \leq t_{\text{th}}, \\ -\frac{I_{\frac{s}{St}-1}[\hat{t}(t)] + d^+ I_{-\frac{s}{St}+1}[\hat{t}(t)]}{I_{\frac{s}{St}}[\hat{t}(t)] + d^+ I_{-\frac{s}{St}}[\hat{t}(t)]}, & t > t_{\text{th}}. \end{cases} \quad (\text{S30})$$

where  $\hat{t} = \sqrt[4]{2^3} \sqrt{\mathcal{A}_{\text{th}}} e^{-|t-t_{\text{th}}|/(2s)} s/St$ . The constants  $c^+$  and  $d^+$  are determined by the initial condition  $\lambda^+(t_0) = (\frac{St}{2s})^2 \hat{t}^2(t_0)$  and by continuity at  $t = t_{\text{th}}$ . For  $\lambda^-$  we find

$$\lambda^-(t) = -\frac{1}{2} + \frac{St}{2s} \hat{t}(t) \times \begin{cases} \frac{J'_{\frac{s}{St}}[\hat{t}(t)] + c^- J'_{-\frac{s}{St}}[\hat{t}(t)]}{J_{\frac{s}{St}}[\hat{t}(t)] + c^- J_{-\frac{s}{St}}[\hat{t}(t)]}, & t \leq t_{\text{th}}, \\ -\frac{J'_{\frac{s}{St}}[\hat{t}(t)] + d^- J'_{-\frac{s}{St}}[\hat{t}(t)]}{J_{\frac{s}{St}}[\hat{t}(t)] + d^- J_{-\frac{s}{St}}[\hat{t}(t)]}, & t > t_{\text{th}}, \end{cases} \quad (\text{S31})$$

$$= \frac{St}{2s} \hat{t}(t) \times \begin{cases} \frac{-J_{\frac{s}{St}+1}[\hat{t}(t)] + c^- J_{-\frac{s}{St}-1}[\hat{t}(t)]}{J_{\frac{s}{St}}[\hat{t}(t)] + c^- J_{-\frac{s}{St}}[\hat{t}(t)]}, & t \leq t_{\text{th}}, \\ -\frac{J_{\frac{s}{St}-1}[\hat{t}(t)] + d^- J_{-\frac{s}{St}+1}[\hat{t}(t)]}{J_{\frac{s}{St}}[\hat{t}(t)] + d^- J_{-\frac{s}{St}}[\hat{t}(t)]}, & t > t_{\text{th}}, \end{cases} \quad (\text{S32})$$

Again, the constants  $c^-$  and  $d^-$  are determined by the initial condition  $\lambda^-(t_0) = -(\frac{St}{2s})^2 \hat{t}^2(t_0)$  and continuity at  $t = t_{\text{th}}$ .

Long observation times,  $|t_0 - t_{\text{th}}| \gg s$ , correspond to  $\hat{t}(t_0) \ll 1$ . In this case, the constants  $c^+$  and  $c^-$  behave asymptotically as

$$c^\pm \sim \pm \frac{St}{s} \left( \frac{\hat{t}^2(t_0)}{4} \right)^{1+s/St} \frac{\Gamma(-\frac{s}{St})}{\Gamma(2 + \frac{s}{St})}. \quad (\text{S33})$$

So that  $c^\pm$  are exponentially small in  $|t_0 - t_{\text{th}}|$ . We then find an approximation for  $d^\pm$  by setting  $c^\pm$  to zero. This gives

$$d^+ \sim -\frac{\frac{d}{dx} J_{\frac{s}{St}}^2(x)}{\frac{d}{dx} (I_{\frac{s}{St}}(x) I_{-\frac{s}{St}}(x))} \Big|_{x=\sqrt[4]{2^3} \sqrt{\mathcal{A}_{\text{th}}} s/St}, \quad d^- \sim -\frac{\frac{d}{dx} J_{\frac{s}{St}}^2(x)}{\frac{d}{dx} (J_{\frac{s}{St}}(x) J_{-\frac{s}{St}}(x))} \Big|_{x=\sqrt[4]{2^3} \sqrt{\mathcal{A}_{\text{th}}} s/St}. \quad (\text{S34})$$

From the properties of the modified Bessel functions  $I_{\frac{s}{St}}$  we find that  $\lambda^+$  is always finite, while  $\lambda^-$  may diverge, because the denominator in Eq. (S31) may become zero for  $t > t_{\text{th}}$ . The threshold value  $\mathcal{A}_{\text{th}}$  is determined by the smallest, non-zero value of  $\mathcal{A}_{\text{th}}$  so that  $\lambda^-(t)$  escapes to negative infinity. An analysis of the denominator of  $\lambda^-$  for  $t > t_{\text{th}}$  using the expression (S34) for  $d^-$  we find that  $\mathcal{A}_{\text{th}}$  is given in terms of the smallest root of  $J'_{\frac{s}{St}}(x)$  by

$$\mathcal{A}_{\text{th}} \sim \frac{St^2}{(2s)^2} \sqrt{2} y^2, \quad \text{where } y \text{ is the smallest solution of } J'_{\frac{s}{St}}(y) = 0. \quad (\text{S35})$$

We have checked that this result agrees well with the numerical value for  $\mathcal{A}_{\text{th}}$  when  $|t_0 - t_{\text{th}}| \ll s$ . When computing the optimal trajectories shown in Fig. (3) in the main text, the threshold value  $\mathcal{A}_{\text{th}}$  must be exceeded slightly, in order to enable  $\lambda^-$  to escape to negative infinity in finite time. The amount by which the threshold is exceeded is a free parameter in our model. Motivated by the fact that fluctuation around the optimal path  $A_{\text{opt}}^i$  are of the order of  $St$  we chose this parameter to be equal to  $St$ .

### III. DIRECT NUMERICAL SIMULATIONS

In this section, we provide some details of the numerical method we used to solve the two-dimensional Navier-Stokes equations and the particle dynamics, resulting in Figs. 2 and 3.

$N$	$f_0$	$k_f$	$\mu$	$\nu$	Re	$N_p$	St	$\Theta$
1024	$5 \times 10^{-3}$	4	$10^{-2}$	$10^{-5}$	1700	$10^5$	0.18	-0.52 10

TABLE I. The parameters used in our DNS of two-dimensional turbulence. For the numerical evolution we use a time step of  $5 \times 10^{-3}$  units and a total simulation time of 400 units. The Kolmogorov time evaluates to  $\tau_K \approx 2.9$  units.

In two spatial dimensions, the incompressible Navier-Stokes equations are conveniently expressed in terms of a stream function  $\psi(\mathbf{x}, t)$  and the fluid vorticity  $\omega(\mathbf{x}, t) = \nabla \times \mathbf{u}(\mathbf{x}, t)$ . Using the stream function  $\psi$ , defined by  $\mathbf{u} = (-\partial_{x_2}\psi, \partial_{x_1}\psi)$ , enforces the incompressibility condition  $\nabla \cdot \mathbf{u} = 0$ . In terms of  $\psi$  and  $\omega = \Delta\psi$ , the two-dimensional Navier-Stokes equations read

$$\partial_t \omega + \partial_{x_1} \psi \partial_{x_2} \omega - \partial_{x_1} \omega \partial_{x_2} \psi = \nu \nabla^2 \omega - \mu \omega + f. \quad (\text{S36})$$

Here  $f$  is a large-scale forcing that generates the turbulence. We take this forcing to be deterministic and time-independent,  $f(\mathbf{x}, t) = f_0 \sin(k_f x_2)$ . The friction term  $-\mu\omega$  in Eq. (S36) ensures a stationary turbulent state. The simulation domain is a square box of side length  $L = 2\pi$  with periodic boundary conditions and we discretise the spatial coordinates at  $N^2$  points.

We evolve a large number  $N_p$  of particle trajectories by solving simultaneously the Navier-Stokes equation (S36), the single-particle dynamics (1), and, along each particle trajectory, the evolution equation (3) for the particle-velocity gradients  $\mathcal{Z}$ . Whenever  $\mathcal{Z}$  exceeds a large negative threshold  $\Theta$ , we record the formation of a caustic. All simulation parameters are summarised in Table I.

- 
- [1] T. Grafke, R. Grauer, and T. Schäfer, J. Phys. A Math. Theor. **48**, 333001 (2015).
  - [2] L. Onsager and S. Machlup, Phys. Rev. **91**, 1505 (1953).
  - [3] P. C. Martin, E. D. Siggia, and H. A. Rose, Phys. Rev. A **8**, 423 (1973).
  - [4] R. Graham and T. Tél, Phys. Rev. Lett. **52**, 9 (1984).